Prediction of Electrodeposition Rates from an Impinging Jet

Qian Li and J. D. A. Walker
Dept. of Mechanical Engineering and Mechanics, Lehigh University, Bethlehem, PA 18015

A mathematical model and numerical algorithm are developed to predict electrodeposition rates from a 2-D jet of electrolyte that impinges on a flat surface. The principal situations of interest are for applied voltages that produce current densities below the limiting current. The motion is assumed to be at high speed with the jet inducing a thin laminar boundary layer on the surface; a progressively thinner concentration layer and an electrochemical double layer near the surface are accounted for. Two cases, corresponding to a submerged and unsubmerged jet, are considered. A boundary integral method is used to compute the current density along the plate in a general iterative numerical procedure coupled to the solution of the hydrodynamic, concentration and electrochemical boundary layers. The results show that relatively high deposition rates occur near the point of impingement and that altering the jet angle relative to the surface influences local electrodeposition rates significantly.

Introduction

In industrial applications of electroplating, selectivity and high speed of deposition are usually important criteria. Impinging jet systems have been of considerable interest for some time (see, for example, Alkire and Chen, 1982; Alkire and Ju, 1987; Chin and Agarwal, 1991), since such configurations offer the promise of high mass-transfer rates, as well as the capability to direct the plating to very specific areas of the workpiece. In a typical impinging-jet system, an anode is located in the jet nozzle, either as a porous screen or as a ring within the nozzle. When a potential difference is applied between the anode and the workpiece (the cathode), ions contained in the jet solution migrate in the electric field, with positively charged ions (cations) being attracted to the cathode. Electrodeposition occurs when the cations acquire electrons at the cathode and are thereby plated out of solution. At the relatively high applied voltages that are necessary to produce limiting current densities, unwanted side reactions can occur that have a deleterious effect on the deposited metal layer. Thus practical applications of electroplating are usually carried out at applied voltages that produce current densities below the limiting current. In such situations, the electrodeposition process in an impinging jet generally involves a complex interplay between the applied electric field, the fluid dynamics, and mass-transfer processes near the cathode, as well as the electrochemical processes in the double layer immediately adjacent to the cathode (Pickett, 1979; Newman, 1991). In the present study, a mathematical formulation has been developed for electrodeposition from an impinging two-dimensional (2-D) jet that floods the workpiece. Numerical solutions have been obtained for an electrochemical solution representative of that used in the electrodeposition of gold on metal surfaces. The influence of directing the jet at different angles to the workpiece is considered and shown to have a significant effect on the distribution of current density at the cathode.

For an aqueous solution containing a dilute concentration of reacting ion, two types of impinging-jet flow may be employed. In the unsubmerged case, the jet is directed at the workpiece but the liquid jet is surrounded by stagnant air; the electrodeposition process is driven in part by the electric field, which is then effectively confined within the jet boundaries. In the submerged case, the jet is immersed in the electrolyte, and in this case the electric field is no longer constrained to be within the jet. Consequently, differences in the current density distribution at the cathode can be expected for each case and both situations will be considered here.

Analysis of impinging jet systems (Alkire and Chen, 1982; Albery, 1985), is usually based on dividing the flow field into

Correspondence concerning this article should be addressed to J. D. A. Walker.

three zones consisting of (1) the free jet region downstream of the nozzle; (2) the stagnation region near the point of impingement; and (3) a "wall jet region" outboard of the stagnation zone. If the jet is supposed to originate from a nozzle of width h above the cathode, let U_o denote the average jet speed at the nozzle, and define a Reynolds number by $Re = U_o h/\nu$, where ν is the kinematic viscosity. Because ν is generally small, typical Reynolds numbers, even for moderate jet speeds, are large. A number of treatments of impinging flow have been based, in part, on a boundary-layer solution obtained for the "wall jet region" by Glauert (1956); this analysis assumes that the volumetric flux in the "wall jet" is small so that the mass flux can be entirely accommodated in a thin laminar boundary layer along the surface. For analysis of devices such as the wall-jet electrode (Yamada and Matsuda, 1973; Alberry, 1985), the assumption of small mass flux may be appropriate since the nozzle diameters are typically very small. However, in the present study, impinging jet flows having significantly higher volumetric flow rates are considered corresponding to situations where the surface is flooded with an excess of electrolyte. The Reynolds number Re is still assumed to be large, but the volumetric flow rate in the jet hU_o is not assumed to be small and is at least $O(1)$.

The situations considered correspond to a plane 2-D jet directed at the surface at an arbitrary angle θ. Since the volumetric flow rate in the jet is not small, the flow splits at the point of impingement and spreads along the surface as an effectively inviscid jet with a speed $O(U_o)$ and a width $O(h)$. Below the inviscid jet flow, a thin hydrodynamic boundary layer develops in order to satisfy the no-slip condition at the surface; in this study the boundary layer is assumed to be laminar. Furthermore, as the reacting ion is consumed at the cathode, a deficiency develops near the cathode, and consequently a diffusion layer must occur there. Because diffusion coefficients for reacting ions in an aqueous solution are usually much smaller than the kinematic viscosity of water, the diffusion layer is generally much thinner than the hydrodynamic layer. Finally, an even thinner electrochemical double layer (Pickett, 1979; Newman, 1991) occurs immediately adjacent to the cathode, and it is here where reactions leading to electrodeposition take place. At current densities below the limiting current, the solution for the electrical potential distribution in the jet is coupled in a complex and nonlinear manner to processes occurring in the hydrodynamic, diffusion, and double layers. Some of the basic features of the interaction have been described by a number of authors for electrodeposition processes occurring in a channel flow with electrodes embedded in the walls (Parrish and Newman, 1969; Caban and Chapman, 1976; Kim and Walker, 1988). Here a more complex geometrical configuration is addressed, with boundaries defined by the perimeter of the jet.

The approach developed here may be applied to a variety of electrodeposition processes, but as an example of a specific application, the process for electroplating of gold is considered; this is carried out extensively in the electronics industry because gold is highly resistant to corrosion and provides high electrical conductivity. Electroplating of gold can be performed from a variety of aqueous solutions containing a variety of additives that are known to have various influences on the deposited metal layer (see, for example, Cheh and Sard, 1971; Bindra et al., 1989), as well as the electrochemical properties of the solution. In general, the aqueous solution contains excess inert electrolyte such as potassium and citrate ions, which do not take part in the reaction at either electrode, but do migrate within the electric field and thereby act to carry the majority of current within the bulk of the solution. Gold is generally present in the solution (Cheh and Sard, 1971) as the negatively charged ion gold dicyanide $Au(CN)_2^-$ and normally may be regarded as a minor ionic component since typical concentrations are 0.1 M. As a gold dicyanide ion approaches the cathode surface, the intense field in the electrochemical double layer acts to promote the forward reaction for

$$Au(CN)_2^- \rightleftarrows AU^+ + 2CN^-. \tag{1}$$

The liberated gold ions are then deposited on the cathode according to the reaction

$$Au^+ + e \rightleftarrows Au, \tag{2}$$

while the cyanide ions combine with hydrogen in solution to form hydrogen cyanide gas. Some evolution of hydrogen gas may also occur at the cathode, but this typically only accounts for 1% or less of the total current. Although the gold dicyanide is a minor ionic component, the current density near the cathode is essentially associated with the reactions in Eq. 2. Since the gold dicyanide ions are negatively charged, they are actually repelled from the cathode by the electric field but reach the cathode through a diffusion layer that develops due to the concentration difference set up as the gold dicyanide ions are depleted from the reaction 1 near the cathode. Thus the overall rate of electrodeposition is controlled by diffusion.

At the anode, the reaction

$$4OH^- \rightarrow O_2 \uparrow + 2H_2O + 4e \tag{3}$$

takes place and results in the evolution of oxygen gas. An alternate way to write a portion of this reaction is

$$2O^{--} \rightarrow O_2 \uparrow + 4e. \tag{4}$$

This process carries the current through the electrochemical layer near the anode and results in a flow of electrons from the solution to the anode. The reaction differs from that at the cathode in the sense that the reactants are abundant in an aqueous solution; consequently, a diffusion layer does not occur near the anode and the current flow across the double layer may be modeled using a standard Butler–Volmer relation (Pickett, 1979).

The objective of this article is to develop a method to predict electrodeposition rates on an infinite flat surface from a 2-D impinging jet oriented at different angles to the surface. The plan of the article is as follows. First the inviscid solution for an impinging thick jet is described. The hydrodynamic boundary layer develops outward from the stagnation region of the jet, and the solution for this layer is obtained numerically. The development of the thinner diffusion layer is controlled both by the viscous shear associated with the hydrodynamic boundary layer above and also by the current flow into

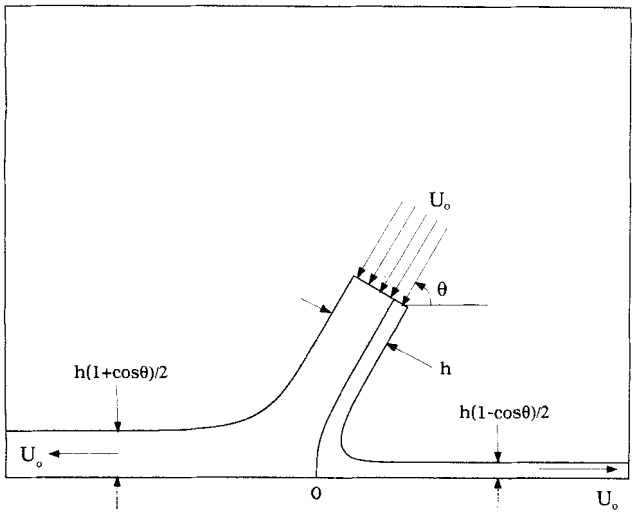

Figure 1. Jet impinging on a flat surface at angle θ.

the diffusion layer. Numerical solutions are obtained for the diffusion layer in a general iterative method, which is coupled with a numerical solution of the Laplace equation governing the potential distribution in the jet and a nonlinear current/overpotential relation modeling the current flow across the electrochemical double layers.

Inviscid Flow for an Impinging Jet

Consider a jet at angle θ that floods a horizontal flat surface as depicted in Figure 1. It is convenient to define dimensionless variables in terms of the jet width h and speed U_o far from the plate, and in this system the jet has a speed and width of unity at infinity. A Cartesian coordinate system (x,y), centered at the stagnation point O of the jet on the surface, is defined measuring dimensionless distance (with respect to h) and having corresponding dimensionless velocity components (u,v) (with respect to U_o). It may be noted that the streamline that impinges on the stagnation point O does not generally coincide with the geometrical centerline of the jet, and for the configuration shown in Figure 1 with $0 < \theta < \pi/2$, more fluid moves to the left along the wall than to the right.

To describe the fluid motion, a streamfunction ψ and velocity potential Φ may be defined by

$$u = \frac{\partial \psi}{\partial y} = \frac{\partial \Phi}{\partial x}, \qquad v = -\frac{\partial \psi}{\partial x} = \frac{\partial \Phi}{\partial y}. \tag{5}$$

The complex potential $\omega = \Phi + i\psi$ describing the inviscid flow associated with the jet may be obtained from results given in Milne-Thomson (1962) and, with some changes in notation, it can be shown that

$$\omega = \frac{1}{\pi}\{(1+\cos\theta)\log(1+\tilde{v}) + (1-\cos\theta)\log(1-\tilde{v}) - \log(1+\tilde{v}e^{-i\theta}) - \log(1+\tilde{v}e^{i\theta})\}. \tag{6}$$

Here $\tilde{v} = u - iv$ is the dimensionless complex velocity, which is given as an implicit function of the complex variable $z = x + iy$ by

$$z = \frac{1}{\pi}\{(1+\cos\theta)\log(1+\tilde{v}) - (1-\cos\theta)\log(1-\tilde{v}) - e^{i\theta}\log(1+\tilde{v}e^{i\theta}) - e^{-i\theta}\log(1+\tilde{v}e^{-i\theta})\}, \tag{7}$$

where throughout "log" denotes the natural logarithm. Equations 6 and 7 define the complex potential ω as an implicit function of z, from which the velocity distribution in the jet can be obtained. Note that as indicated in Figure 1, the jet bifurcates at the stagnation point and then (in dimensionless variables) accelerates to uniform jets of unit speed and width $(1 \pm \cos\theta)/2$ as $x \to \pm\infty$, respectively.

Two features of the inviscid jet solution are needed, namely: (1) the equation of the jet boundary, and (2) the tangential velocity $U_e(x)$ induced by the jet near the surface. The latter quantity is obtained by taking the limit $y \to 0$ in Eq. 7, for which $z \to x$ and $\tilde{v} \to U_e(x)$, and it is easily shown that

$$\pi x = (1+\cos\theta)\log\{1+U_e\} - (1-\cos\theta)\log\{1-U_e\} - \cos\theta \times \log\{1+U_e^2+2U_e\cos\theta\} + 2\sin\theta\tan^{-1}\left\{\frac{U_e\sin\theta}{1+U_e\cos\theta}\right\}. \tag{8}$$

This transcendental equation implicitly defines U_e as a function of x. For a given value of x, Eq. 8 may be solved numerically for U_e and distributions for various jet angles θ are shown in Figure 2. Note that $U_e \to \pm 1$ as $x \to \pm\infty$, respectively, and that near the stagnation point,

$$U_e(x) \sim a_1 x \quad \text{as} \quad x \to 0, \tag{9}$$

where $a_1 = \pi/(4\sin^2\theta)$. Consequently, as the jet angle θ decreases, the variation in U_e becomes progressively more intense near the stagnation point, as shown in Figure 2.

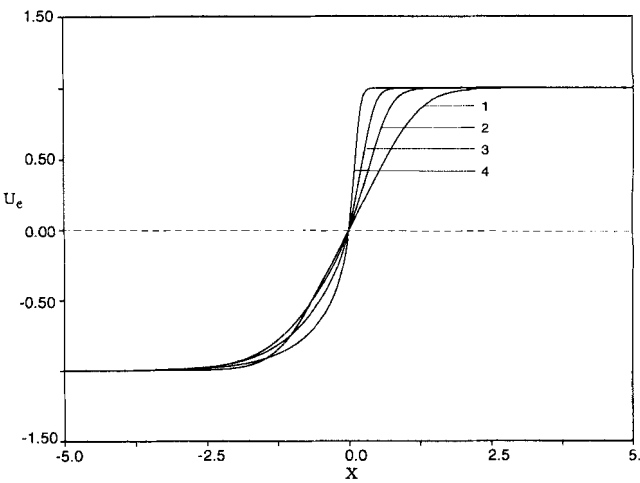

Figure 2. Mainstream velocity distribution near the surface for jet angles: (1) $\theta = 90°$; (2) $\theta = 60°$; (3) $\theta = 45°$; (4) $\theta = 30°$.

The equation of the jet boundary is obtained by noting that along the free streamlines the flow speed is constant, and in dimensionless variables the complex velocity is $\bar{v} = e^{-i\gamma}$, where γ is a variable denoting the angle the velocity vector makes with the horizontal. Substitution in Eq. 7 yields parametric equations for the jet boundary according to

$$\pi x = (\theta - \pi\delta)\sin\theta + (1+\cos\theta)\log|\cos(\gamma/2)| - (1-\cos\theta) \times \log|\sin(\gamma/2)| - \cos\theta \log\left|\cos\left(\frac{\theta+\gamma}{2}\right)\cos\left(\frac{\theta-\gamma}{2}\right)\right|, \quad (10)$$

$$\pi y = \frac{\pi}{2}\{1+(2\delta-1)\cos\theta\} + \sin\theta\left\{\log\left|\cos\left(\frac{\theta+\gamma}{2}\right)\right| - \log\cos\left|\left(\frac{\theta-\gamma}{2}\right)\right|\right\}. \quad (11)$$

Here $\delta = 0$ if $\gamma \geq \theta - \pi$ and $\delta = 1$ if $\gamma < \theta - \pi$. Along the jet boundary to the left in Figure 1, the angle γ varies from $\gamma = -\pi$ as $x \to -\infty$ to $\gamma = -\theta$; on the jet boundary to the right γ varies from $\gamma = -\theta$ to $\gamma = 0$ as $x \to \infty$.

The Hydrodynamic Boundary Layer

The situations of interest here correspond to high-speed flow in the sense that $Re = U_o h/\nu$ is assumed to be large; in such circumstances, the tangential velocity induced by the jet is reduced to relative rest on the plate through a thin hydrodynamic boundary layer below the jet. The boundary layer is assumed to be laminar with thickness $O(Re^{-1/2})$ and is therefore described by the scaled variables.

$$v = Re^{-1/2}\bar{v}, \qquad y = Re^{-1/2}Y, \qquad \psi = Re^{-1/2}\Psi, \quad (12)$$

where the streamfunction ψ is defined in Eq. 5. The 2-D boundary-layer equations may then be written

$$u\frac{\partial u}{\partial x} + \bar{v}\frac{\partial u}{\partial Y} = U_e\frac{dU_e}{dx} + \frac{\partial^2 u}{\partial Y^2}, \qquad \frac{\partial u}{\partial x} + \frac{\partial \bar{v}}{\partial Y} = 0, \quad (13)$$

with boundary conditions

$$u(x,0) = \bar{v}(x,0) = 0, \qquad u \to U_e(x) \quad \text{as} \quad y \to \infty. \quad (14)$$

The boundary layer is very thin with respect to the vertical dimensions of the jet and originates at the stagnation point O shown in Figure 1. To calculate the boundary-layer solution, it is convenient to introduce the Levy–Lees transformation (Cebeci and Smith, 1974, p. 260) according to

$$\xi = \int_0^x U_e(t)\,dt, \qquad \eta = \frac{|U_e(x)|}{\sqrt{2|\xi|}}Y, \qquad f = \frac{\Psi}{\sqrt{2|\xi|}}. \quad (15)$$

Since $u = \partial\Psi/\partial Y$ and $\bar{v} = -\partial\Psi/\partial x$, it may be easily shown that system 13 becomes

$$\frac{\partial^3 f}{\partial\eta^3} + f\frac{\partial^2 f}{\partial\eta^2} + q\left[1 - \left(\frac{\partial f}{\partial\eta}\right)^2\right] = 2\xi\left[\frac{\partial f}{\partial\eta}\frac{\partial^2 f}{\partial\xi\partial\eta} - \frac{\partial f}{\partial\xi}\frac{\partial^2 f}{\partial\eta^2}\right], \quad (16)$$

with

$$f = \frac{\partial f}{\partial\eta} = 0 \quad \text{at} \quad \eta = 0; \qquad \frac{\partial f}{\partial\eta} \to 1 \quad \text{as} \quad \eta \to \infty, \quad (17)$$

and the pressure gradient parameter $q(\xi)$ is defined by

$$q(\xi) = \frac{2\xi}{U_e}\frac{dU_e}{d\xi}. \quad (18)$$

The boundary-layer flow develops in the $\pm\xi$ directions away from the stagnation point at $\xi = 0$. Using Eq. 9, it is easily shown that $q \to 1$ as $\xi \to 0$; consequently, Eq. 16 reduces to a Falkner-Skan equation, viz.,

$$f''' + ff' + 1 - f'^2 = 0, \quad (19)$$

describing the initial velocity profile at the stagnation point O; here the primes denote differentiation with respect to η.

The solution of the system (Eqs. 16 and 17) may easily be constructed for a given jet angle θ by first calculating the stagnation point profile described by Eq. 19. A boundary-value procedure was used (Werle and Davis, 1972; Walker and Weigand, 1979) using typically 150 points across the boundary layer and applying the last of conditions 17 at $\eta = 10$ as an approximation. A number of mesh sizes were used as a check on the accuracy and the presented results are believed to be grid independent. A Crank–Nicholson method (Werle and Davis, 1972; Smith, 1985) was then used to construct the boundary-layer solution for both $\xi > 0$ and $\xi < 0$ by marching away from the stagnation point. A typical value $\Delta\xi = 0.0004$ for the mesh size in the ξ direction was used in the vicinity of the stagnation point because of the intense variation of the solution there, especially for decreasing θ. Larger values of $\Delta\xi$ could then be used with good accuracy at locations remote from the impingement zone.

Calculated values of the dimensionless wall shear stress β, defined by

$$\beta = \left.\frac{\partial u}{\partial Y}\right|_{Y=0} = \frac{U_e|U_e|}{\sqrt{2|\xi|}}\left.\frac{\partial^2 f}{\partial\eta^2}\right|_{\eta=0}, \quad (20)$$

are shown in Figure 3 for various jet angles. As $\xi \to \pm\infty$, the jet returns to a uniform flow and the shear stress must approach the Blasius solution for a flat-plate boundary layer (White, 1992), viz.,

$$\beta \sim \pm\frac{\beta_\infty}{\sqrt{|x|}} \quad \text{as} \quad x \to \pm\infty, \quad (21)$$

where $\beta_\infty = 0.332$. As shown in Figure 3, the shear stress rapidly approaches the Blasius asymptotic forms 21 outside the immediate vicinity of the impingement zone. As anticipated from Eq. 9, the variation in shear stress becomes progressively more intense near 0 as the jet angle θ is decreased; in fact, it is easily shown that

$$\beta \sim \beta_o x + \ldots \quad \text{as} \quad x \to 0, \quad (22)$$

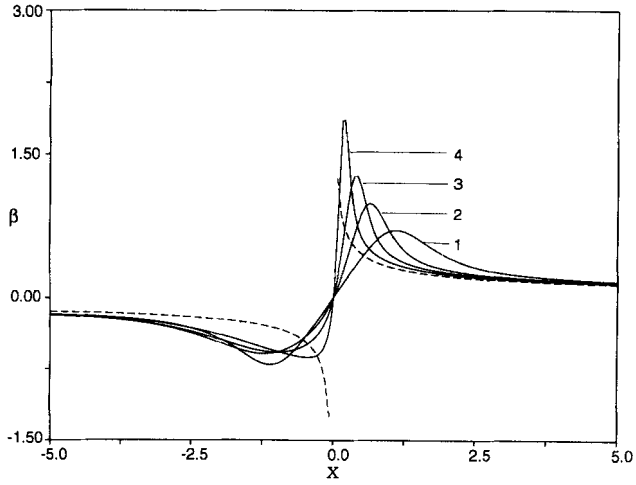

Figure 3. Dimensionless surface shear stress for jet angles: (1) $\theta = 90°$; (2) $\theta = 60°$; (3) $\theta = 45°$; (4) $\theta = 30°$; ----- Blasius solution.

where the constant $\beta_o = 1.2326 a_1^{3/2}$ and $a_1 = \pi/(4\sin^2\theta)$. This trend has important consequences since the shear imposed on the concentration layer has a strong influence on the mass transfer at the surface.

Diffusion Layer

For a dilute solution, incompressible liquid containing M ionic species, conservation of species requires (Pickett, 1979)

$$(\mathbf{v}^* \cdot \nabla) c_j = D_j \nabla^2 c_j + \frac{Z_j F D_j}{RT} \nabla \cdot (c_j \nabla \phi^*), \qquad j = 1, 2, \ldots, M, \tag{23}$$

where c_j, D_j, and Z_j are the concentration, diffusion coefficient, and valence of the j^{th} ionic species; in addition, F is Faraday's constant, R is the gas constant, T is the temperature, $\mathbf{v}^*$ is the dimensional solution velocity vector, ϕ^* is the potential distribution, and ∇ is the 2-D gradient operator. The electrodeposition process is driven by an applied potential difference between the anode and the flat plate, which is assumed to be the cathode at zero potential. Electrochemical solutions often contain supporting electrolyte consisting of a variety of ionic species that do not take part in the reaction at the cathode. These ions are referred to as excess electrolyte; they serve to enhance the solution conductivity and carry the current flow in the bulk of the fluid via a process of migration in the electric field. In this study, it is assumed there is one reacting ion that has a uniform but small concentration $c_{1\infty}$ within the jet; this ion is $Au(CN)_2^-$ for the electrodeposition of gold from an aqueous solution and may be considered a minor ionic component. Under such circumstances, migration in the diffusion layer can be neglected (Newman, 1967, 1991). Since the concentration of the reacting ion is depleted near the cathode as a consequence of the reaction, a concentration gradient develops and gives rise to mass transfer near the electrode. In a typical aqueous solution at room temperature, the kinematic viscosity $\nu = 1 \times 10^{-2}$ cm^2/s, while values of the diffusion coefficient D_1 are usually much smaller (Alkire and Chen, 1982) and on the order of 10^{-5}cm^2/s. Thus the Schmidt number $Sc = \nu/D_1$ is typically large, and the mass transfer takes place in a diffusion layer, which is thin with respect to the hydrodynamic boundary layer. Consequently, for $Sc \gg 1$ the velocity distribution in the diffusion layer is described by the solution of Eq. 16 evaluated for small Y according to

$$u = \beta(x) Y + \ldots, \qquad \bar{v} = -\beta'(x) \frac{Y^2}{2} + \ldots, \quad \text{as} \quad Y \to 0, \tag{24}$$

where β is calculated from Eq. 20. Using Eq. 12 and introducing scaled dimensionless variables for the diffusion layer by

$$c = \frac{c_1}{c_{1\infty}}, \qquad \bar{y} = Sc^{1/3} Re^{1/2} y = Sc^{1/3} Y, \tag{25}$$

it may easily be confirmed that Eq. 23 reduces to

$$\beta \bar{y} \frac{\partial c}{\partial x} - \frac{1}{2} \beta' \bar{y}^2 \frac{\partial c}{\partial \bar{y}} = \frac{\partial^2 c}{\partial \bar{y}^2}, \tag{26}$$

to leading order for $Sc \gg 1$, when the effects of migration are negligible in the diffusion layer. Thus the principal balance occurs between the convective terms in Eq. 23 and diffusion normal to the wall. One boundary condition for Eq. 26 expresses the fact that c_1 must return to the bulk value $c_{1\infty}$ at the outer edge of the diffusion layer, viz.,

$$c(x, \bar{y}) \to 1 \quad \text{as} \quad \bar{y} \to \infty. \tag{27}$$

A second condition at $\bar{y} = 0$ must be obtained through consideration of conservation of ionic flux near the surface.

As a useful basis of comparison, consider first the limiting current distribution, which occurs when the applied potential is sufficiently large so that the reacting ions are immediately consumed upon arriving at the inner edge of the diffusion layer, viz.,

$$c(x, 0) = 0 \quad \text{for all } x. \tag{28}$$

Introducing the transformations due to Lighthill (1950) (see also Acrivos (1960))

$$\bar{\xi} = w(x), \qquad \zeta = \bar{y} \beta^{1/2}(x)/w(x), \tag{29}$$

where

$$w(x) = \left\{ 9 \int_0^x \beta^{1/2}(t) dt \right\}^{1/3}, \tag{30}$$

it may be easily confirmed that Eq. 26 becomes

$$\frac{\partial^2 c}{\partial \zeta^2} + 3\zeta^2 \frac{\partial c}{\partial \zeta} = 3\bar{\xi} \zeta \frac{\partial c}{\partial \bar{\xi}}. \tag{31}$$

The solution satisfying conditions 27 and 28 is

$$c_{\text{lim}}(\zeta) = \frac{1}{\Gamma(4/3)} \int_0^{\zeta} e^{-t^3}\, dt, \tag{32}$$

where c_{lim} denotes the concentration distribution at the limiting current and $\Gamma(4/3) = 0.8929\ldots$ is the gamma function.

Since Re is large, the thicknesses of the hydrodynamical and diffusion layers are very small on the scale of the bulk flow in the jet. Within the jet, the current density i is due to migration of ions in the electric field and is carried principally by the supporting electrolyte. Just outside the hydrodynamic boundary layer, i is given by

$$i(x) = -\frac{\sigma}{h} \left.\frac{\partial \phi^*}{\partial y}\right|_{y \to 0}, \tag{33}$$

where σ is the solution conductivity and the factor h results from the nondimensionalization of y. Nearer the surface and at the base of the concentration layer, the current is due to mass transfer of the reacting ion (to leading order) and is given by (Pickett, 1979)

$$i = -\frac{D_1 Z_1 F}{h} \left.\frac{\partial c_1}{\partial y}\right|_{y \to 0}. \tag{34}$$

Introducing the dimensionless variables defined in Eq. 25, it follows that

$$i(x) = -I_o \left.\frac{\partial c}{\partial \bar{y}}\right|_{\bar{y} = 0}, \tag{35}$$

where I_o is a representative current density defined by

$$I_o = \frac{D_1 Z_1 F c_{1\infty}}{h} Sc^{1/3}\, Re^{1/2}, \tag{36}$$

From Eq. 32 the limiting current distribution is given by

$$\frac{i_{\text{lim}}(x)}{I_o} = -\frac{\beta^{1/2}(x)}{\Gamma(4/3) w(x)}, \tag{37}$$

and three features are worthy of note. First, the increasingly intense variation of the wall shear β in the impingement zone (Figure 3) for decreasing angles θ implies a similar behavior in $i_{\text{lim}}(x)$. Second, it follows from Eqs. 22 and 30 that near the stagnation point

$$i_{\text{lim}}(x) \sim -\frac{I_o}{\Gamma(4/3)} \left(\frac{\beta_o}{6}\right)^{1/3} \quad \text{as} \quad x \to 0. \tag{38}$$

Thus relatively higher levels of limiting current occur near O with decreasing jet angles θ since β_o then increases. Last, it follows from Eq. 21 that far from the impingement zone

$$i_{\text{lim}}(x) \sim -\frac{I_o}{\Gamma(4/3)} \left(\frac{\beta_\infty}{12}\right)^{1/3} \frac{1}{|x|^{1/2}} \quad \text{as} \quad |x| \to \infty, \tag{39}$$

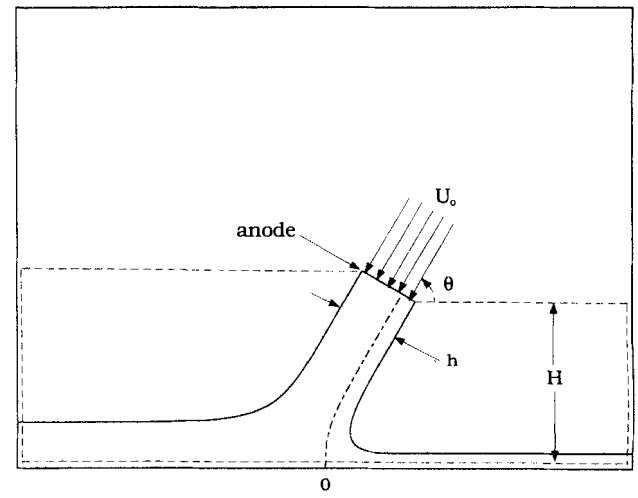

Figure 4. Computational domain.

and consequently the limiting current decays very slowly with distance from the origin. These general characteristics will subsequently be illustrated in Figure 5.

The high applied potential differences needed to produce electrodeposition rates near the limiting current also tend to induce unwanted side reactions, and for this reason typical electroplating cells are operated at lower voltages. Within these ranges, the solution of the diffusion layer is coupled to the potential distribution outside the boundary layers, since the current density just outside the concentration layer given by Eq. 33 must balance that given by Eq. 35 into the electrochemical double layer. Defining a dimensionless potential ϕ by

$$\phi = \frac{\phi^* Z_1 F}{RT}, \tag{40}$$

it follows that the boundary condition for the concentration near the surface is

$$\left.\frac{\partial c}{\partial \bar{y}}\right|_{\bar{y} = 0} = I(x). \tag{41}$$

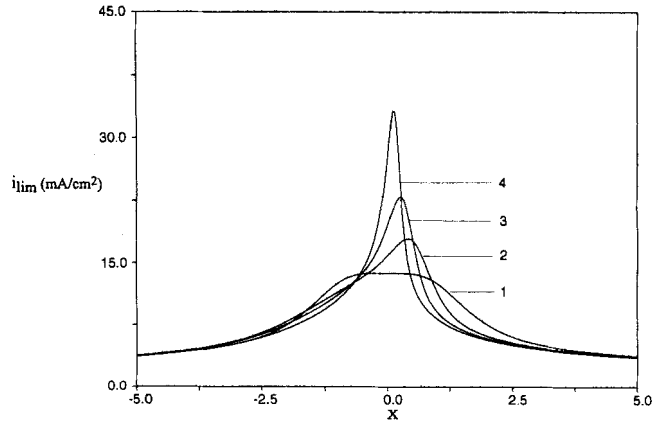

Figure 5. Limiting current distribution on the cathode for $Re = 10^4$ and for (1) $\theta = 90°$; (2) $\theta = 60°$; (3) $\theta = 45°$; (4) $\theta = 30°$.

Here $I(x)$ is a dimensionless current related to the potential gradient near the surface by

$$I(x) = -\frac{i}{I_o} = Q\left.\frac{\partial \phi}{\partial y}\right|_{y=0}, \tag{42}$$

where the dimensionless parameter Q is defined by

$$Q = \frac{\sigma RT\, Re^{1/2}\, Sc^{2/3}}{h(Z_1F)^2 c_{1\infty} U_o}. \tag{43}$$

For a given applied potential, the dimensionless current $I(x)$ along the plate is unknown and must be found in a general iterative numerical scheme, involving computation of the potential ϕ is the bulk flow and, in particular, the flux in Eq. 42. The procedure for evaluating ϕ is described in the next section; here it is assumed that an estimate of the distribution of $I(x)$ is available from a previous iteration, and the objective is to calculate a solution of Eq. 26 subject to conditions 27 and 41. The important result obtained from this calculation is the dimensionless surface concentration of the reacting ion, subsequently denoted as $c_s(x) = c(x,0)$.

The diffusion layer also originates at the stagnation point O and since $\beta \to 0$ as $x \to 0$, Eq. 26 reduces to the ordinary differential equation

$$\frac{d^2c}{d\bar{y}^2} + \frac{1}{2}\beta_o \bar{y}^2 \frac{dc}{d\bar{y}} = 0. \tag{44}$$

The solution of this equation satisfying conditions 27 and 41 is

$$c(0,\bar{y}) = 1 - I(0)\int_{\bar{y}}^{\infty} e^{-\beta_o t^3/6}\, dt, \tag{45}$$

where $I(0)$ denotes the value of the dimensionless current at the stagnation point. At the wall, the surface concentration at the stagnation point O is

$$c_s(0) = 1 - \left(\frac{6}{\beta_o}\right)^{1/3} \Gamma(4/3)\, I(0). \tag{46}$$

Note that $I(0)$ is not known *a priori* and must be found in a general iterative scheme described in the next section. For relatively low levels of applied potential, $I(0)$ is small and the surface concentration is close to one; however, with increasing applied potential, $I(0)$ increases and the concentration of the reacting ion is significantly reduced near the electrode. It is noted in passing that the limiting current at the stagnation point itself is reached when $c_s = 0$. For a normal jet ($\theta = \pi/2$), the minimum concentration and maximum current density both occur at $x = 0$, and the maximum dimensionless current density follows from Eq. 47 and is $I(0) = 0.5856$.

To compute the surface concentration for all x, it is necessary to initiate a numerical integration of Eq. 26 in the directions of both positive and negative x. For a given jet angle, the shear stress distribution $\beta(x)$ is known from the hydrodynamic boundary-layer calculations and an estimate of $I(x)$ is assumed to be available from a previous iteration; note that some care is necessary in selecting the initial guess for $I(x)$ to ensure that a negative value of c_s is not obtained at $x = 0$. The solution may then be constructed in a step-by-step manner using a Crank–Nicolson method with second-order accurate central differencing for both Eq. 26 and the derivative boundary condition 41. In a typical calculation, 150 points were used across the diffusion layer and condition 27 was applied at $\bar{y} = 10$ as an approximation. The streamwise variation of the ionic concentration near 0 can be intense, and small mesh sizes in Δx are necessary to ensure a smooth and grid-independent solution; typical values of Δx used for the diffusion layer were ten times smaller than in the hydrodynamic boundary-layer calculation. Discussion of specific results will follow subsequently.

Evaluation of the Potential

In the bulk flow in the jet, the potential ϕ satisfies the Laplace equation $\nabla^2\phi = 0$. The present configuration is shown in Figure 4 where an anode, of dimensionless length h and oriented perpendicular to the flow of the jet, is at a dimensionless distance H from the plate. The length scale used to nondimensionalize the equations is based upon the inviscid solution for the jet thickness at a large distance from the surface; thus the dimensionless anode length h is somewhat larger than one, and as H increases, h decreases monotonically to unity. The anode may be considered to be part of the jet nozzle and/or a screen through which the jet flows. At both the anode and cathode, a jump in potential occurs across a thin electrochemical double layer, and kinetic relations are required to relate these jumps in potential to the current flow across the double layers.

Since a concentration layer occurs on the cathode, the kinetic relation must reflect the change in concentration (from the bulk value) near the cathode. The current/overpotential relation used in the present study at the cathode is of the form (see, for example, Pickett, 1979)

$$-\sigma\frac{\partial \phi^*}{\partial n^*} = i_o^*\left[c_s(x)\exp\left\{-\frac{\alpha Z_1 F\eta'}{RT}\right\} - \exp\left\{\frac{(1-\alpha)Z_1F\eta'}{RT}\right\}\right]. \tag{47}$$

Here n^* denotes the outward normal direction to the computational boundary, which is shown as a broken line in Figure 4; in addition, α, i_o^*, and Z_1 are the transfer coefficient, exchange current density, and number of electrons exchanged in the reaction at the cathode, all of which are characteristic of the electroplating cell; η' is the total overpotential defined by $\eta' = -\phi^*(x,0^+)$, since the cathode itself is assumed at zero potential. Here $\phi^*(x,0^+)$ denotes the potential in solution just outside the diffusion layer on the cathode. Introducing a dimensionless distance $n = n^*/h$ and the dimensionless potential ϕ in Eq. 40, Eq. 47 may be written in the form

$$-\frac{\partial \phi}{\partial y} = \frac{\partial \phi}{\partial n} = -i_o\{c_s\exp(\alpha\phi) - \exp[-(1-\alpha)\phi]\}, \tag{48}$$

where i_o is a dimensionless exchange current density at the cathode defined by $i_o = (i_o^* hZ_1F/\sigma RT)$. Here y measures di-

mensionless distance away from the cathode and n toward it. It should be emphasized that η' denotes the total overpotential in the kinetic relation 47, which is one of a class of formulas that can be used to model current flow across the double layer (Vetter, 1967; Pickett, 1979; Newman, 1991). Newman (1991) prefers to split the total overpotential into a surface and concentration overpotential, and uses a kinetic relation that is slightly different from Eq. 47. Note however that the kinetic relation utilized by Parrish and Newman (1969), for example, reduces to formula 47 for a situation having zero transference number for the reacting ion.

The electrodeposition of gold from an aqueous solution involves the evolution of oxygen gas at the anode, and since the reactant is plentiful, the current/overpotential relation may be modeled by a standard Butler–Volmer relation (Pickett, 1979; Newman, 1991), which in dimensionless variables is of the form

$$\frac{\partial \phi}{\partial n} = \tilde{i}_o\{\exp(\tilde{a}\tilde{\eta}') - \exp[-(1-\tilde{\alpha})\tilde{\eta}']\}, \qquad (49)$$

where

$$\bar{\alpha} = \tilde{\alpha}\tilde{Z}/Z_1, \qquad \tilde{i}_o = \tilde{i}_o^* \frac{hZ_1F}{\sigma RT}. \qquad (50)$$

Here $\tilde{\alpha}$, $\tilde{Z}$, and $\tilde{i}_o^*$ are the transfer coefficient, number of electrons exchanged in the reaction, and exchange current density at the anode, respectively. In addition, $\tilde{\eta}'$ is the total dimensionless overpotential at the anode defined by $\tilde{\eta}' = V - \phi(x,0^+)$, where $V = V_{app}Z_1F/RT$ is the total dimensionless applied potential (between anode and cathode), and $\phi(x,0^+)$ denotes the dimensionless potential in solution just outside the electrochemical double layer on the anode.

It is convenient to use the boundary integral method to solve the potential problem, since the geometrical domain shown in Figure 4 is complicated, and the principal interest is in the current distribution just outside each electrode (as opposed to within the jet itself). A solution of Laplace's equation satisfies the following integral equation (Jaswon and Symm, 1977).

$$\phi(x_i,y_i) = \frac{1}{\pi}\oint_C \left\{\phi \frac{\partial}{\partial n}(\log r) - \log r \frac{\partial \phi}{\partial n}\right\} ds, \qquad (51)$$

where C is the curve bounding the computational domain in Figure 4 and (x_i,y_i) is any point on that curve. The computational domain depends on whether the jet is submerged or unsubmerged. In both cases the curve C passes just outside the double layers on the electrodes and also crosses the jet normal to the flow direction. For the unsubmerged jet, C passes along the upper boundaries of the jet while the broken line shown in Figure 4 was used for C in the submerged case. In Eq. 51, r denotes the distance from (x_i,y_i) to any point on C and s measures distance in a counterclockwise direction along C.

The classic boundary integral method was used to solve Eq. 51, wherein the curve C is discretized by selecting a finite number of N points along C to represent the computational boundary by a total of N segments. In this method, ϕ and the normal derivative $\partial\phi/\partial n$ (subsequently denoted by ϕ') are taken constant along the jth segment and equal to their values at the segment midpoint. This leads to a system of equations of the form (Jaswon and Symm, 1977):

$$A_{ij}\phi_j + B_{ij}\phi_j' = 0, \qquad i = 1, 2, \ldots, n, \qquad (52)$$

obtained by collocating the approximations to Eq. 51 at the midpoint of each segment. Note that the repeated indices in Eq. 52 imply a summation over all segments. The matrices A_{ij} and B_{ij} depend only on the geometry and have the components

$$A_{ij} = \psi_{ij}^* - \pi\delta_{ij}, \qquad B_{ij} = a\cos\beta_{ij}^* \log\left(\frac{a}{b}\right) - c(\log b - 1) + a\psi_{ij}^* \sin\beta_{ij}^*, \qquad (53)$$

where δ_{ij} is the Kronecker delta; a, b, and c denote the magnitude of the vectors

$$\mathbf{a} = \mathbf{r}_i - \mathbf{r}_j, \qquad \mathbf{b} = \mathbf{r}_i - \mathbf{r}_{j+i}, \qquad \mathbf{c} = \mathbf{r}_{j+i} - \mathbf{r}_j, \qquad (54)$$

with $\boldsymbol{r}_j$ being the radius vector to the jth nodal point on C. The angles ψ_{ij}^* and β_{ij}^* are given by

$$\beta_{ij}^* = \cos^{-1}\left\{\frac{\mathbf{a}\cdot\mathbf{c}}{ac}\right\}, \qquad \psi_{ij}^* = \cos^{-1}\left\{\frac{\mathbf{a}\cdot\mathbf{b}}{ab}\right\}. \qquad (55)$$

It is evident that the matrices A_{ij} and B_{ij} depend only on the geometry considered.

The set of Eqs. 52 defines N relations between the ϕ_j and ϕ_j'. Along the jet boundary $\phi_j' = 0$ and ϕ is unknown while the nonlinear relations 48 and 49 must be satisfied along the electrodes. It follows that Eq. 52 may be rewritten as

$$A_{ij}\phi_j + B_{ij}g(\phi_j) = 0, \qquad (56)$$

where $g(\phi_j)$ denotes either the right side of either of Eqs. 48 or 49 and is zero along the jet boundary. The nonlinear system (Eq. 56) may be written in vector form as $\boldsymbol{F}(\boldsymbol{\phi}) = 0$, where $F_i = A_{ij}\phi_j + B_{ij}g(\phi_j)$, and a Newton–Raphson method with damping was found to be an effective means to solve this system. The Jacobian matrix $J(\boldsymbol{\phi})$ has components $J_{ij} = \partial F_i/\partial\phi_j$, and from Eqs. 48 and 49

$$J_{ij} = A_{ij} + B_{ij}g', \qquad (57)$$

for $i, j = 1, 2, \ldots, N$, where

$$g' = -i_o\{\alpha c_s(x)\exp(\alpha\phi_j) + (1-\alpha)\exp[-(1-\alpha)\phi_j]\}, \qquad (58)$$

for values of j associated with the cathode. For points on the anode, i_o and α are replaced by their counterparts $\tilde{i}_o$ and $\bar{\alpha}$, c_s is set equal to one, and ϕ_j is replaced by $V - \phi_j$ in Eq. 58; on the jet boundary $g' = 0$, note that a term involving $\partial c_s/\partial\phi$ is omitted in Eq. 58 as an approximation, since it is difficult to evaluate and, in addition, during an iterative cycle for the

solution of the Laplace equation, the distribution of $c_s(x)$ was held fixed.

The objective in the Newton–Raphson algorithm is to force the components of $F(\phi)$ to approach zero, and this was done iteratively starting from an initial guess for the ϕ_j by successively recalculating ϕ according to

$$\phi_j^{k+1} = \phi_j^k - J_{ij}^{-1} F_j(\phi^k), \tag{59}$$

where the superscript k denotes the iteration number and J_{ij}^{-1} is the inverse of the Jacobian matrix. Note that in some circumstances, particularly for cases near the limiting current, the step predicted by Eq. 59 may be too large and divergence of the scheme can occur. In such situations, it is necessary to insert a factor ϵ in front of the second term on the right side of Eq. 59, where $0 < \epsilon < 1$; this process is known as *damping* and acts to restrict the step length to avoid divergence at any stage of the iteration. Once a new iterate for the potential distribution along the plate is obtained from Eq. 59, the concentration problem, described in the previous section, must be computed again to obtain a new iterate for $c_s(x)$. Typically twenty global iterations were required to obtain convergence in ϕ and $c_s(x)$ to five significant figures.

The classic method is the simplest of a class of 2-D boundary element methods, but is known to produce oscillations in the flux near corners of the boundary contour. Improved methods for dealing with corners have recently been described by Gray and Manne (1993) and Gray (1994). In present configuration, corners occur where the contour cuts the jet and where the fluxes are generally small. Since the corners are far from the impingement zone, the influence of any deficiencies in the classic method are not believed to be significant for the calculated results near O.

Calculated Results

The electrodeposition problem formulated in this study contains six independent dimensionless parameters, namely, the Reynolds number Re, the Schmidt number Sc, the dimensionless parameters Q, i_o, and $\bar{i}_o$ and the dimensionless distance from the surface of the anode (shown in Figure 4). Provided H is $O(1)$ or larger, the direct influence of the anode and the reaction that occurs there is not particularly significant; insofar as the reaction at the cathode is concerned, the anode is a distant source of positive potential. Of the remaining parameters, the dimensionless exchange current density i_o is mainly dependent on the electrolyte and the specific reaction at the electrode, while Q depends on both the electrolyte and the flow and mass-transfer processes. For the present theory to apply, both Re and Sc must be large. Calculations were carried out for a number of different cases; the results described in this section are based on the parameters listed in Table 1, which are believed to be representative of those associated with electrodeposition of gold from a citrate bath (Kim and Walker, 1988); the value of the dimensionless exchange current density at the cathode is fixed at $i_o = 6.7 \times 10^{-3}$ for all calculations.

It follows from Table 1 that $Sc = 833$ while $Re = 10^4$ and $Q = 0.026$. Calculated results for the limiting current distributions in Eq. 37 are shown in Figure 5 for various jet angles. Here and in subsequent figures, the magnitude of the current

Table 1. Parameters Associated with Gold Electrodeposition

Kinetic Parameters	α	$i_o^*(A/cm^2)$	Z
Cathode	0.406	2.066×10^{-5}	1
Anode	0.113	8.578×10^{-8}	2

Diffusion coefficient	D_1	$= 1.2 \times 10^{-5}$ cm^2/s
Solution temperature	T	$= 298$ K
Solution conductivity	σ	$= 0.122\ \Omega^{-1} \cdot$ cm^{-1}
Solution density	ρ	$= 0.997$ g$\cdot$cm^{-3}
Kinematic viscosity	ν	$= 0.01$ cm^2/s
Jet width	h	$= 1$ cm
Jet speed	U_o	$= 100$ cm/s
Gold dicyanide concentration	$c_{1\infty}$	$= 1 \times 10^{-4}$ mol/cm^3

is plotted. Note that the maximum current density levels increase near O with decreasing jet angle, while the distribution of i becomes more concentrated in the region of the stagnation point. This behavior is directly associated with the increased magnitude and concentrated nature of the dimensionless shear stress β shown in Figure 3 that occurs near the impingement point for decreasing θ. It is also evident from Eq. 36 and 37 that increasing values of the Reynolds number Re gives an increased level of limiting current, since i_{lim} is proportional to $Re^{1/2}$; this behavior is in agreement with the experiments of Chin and Agarwal (1991).

Results were calculated for various values of Re but only those for $Re = 10^4$ will be shown; these are broadly the same as those for larger Re. In practice, for the configuration shown in Figure 1, Re may be increased by increasing the jet speed U_o for a fixed jet width, since the properties ν and D_1 are essentially constant for a given solution. The present theory applies only for large Re.

The flux of reacting ion within the jet is $O(U_o c_{1\infty})$, while the current at the surface is $O(I_o)$, as shown in Eq. 35. Therefore at any station x along the wall, the percentage depletion d of the reacting ion has

$$d = O\left(\frac{I_o}{U_o c_{1\infty}}\right) = O(Z_1 F Sc^{-2/3} Re^{-1/2}) \tag{60}$$

and, consequently, $d \to 0$ for $Re \to \infty$ and $Sc \gg 1$; thus the concentration of the reacting ion remains constant within the jet provided $Re \gg 1$. Once Re is sufficiently large, the distribution of computed results for i/I_o was found to be essentially the same, indicating an independence of Re (although actual levels of i continually increase with Re).

Calculated results for the current density distribution on the plate and the surface concentration of the reacting ion are shown in Figure 6 for an unsubmerged jet that is directed normal to the surface. The current density is largest immediately beneath the anode as expected; however, a region of significant current density occurs outside the horizontal extent of the anode (which is just greater than one unit). A typical characteristic of this type of system is that relatively little current flows until the applied potential is sufficiently large so that the potential just outside the double layer on the cathode is large enough to overcome the small value of i_o in Eq. 48. Then, over a relatively narrow range of applied potential V, there is a current flow that soon approaches levels close to the limiting current near the origin. The corresponding calculated results for surface concentration are shown in Figure 6b. At very low values of V, $c_s(0)$ is almost

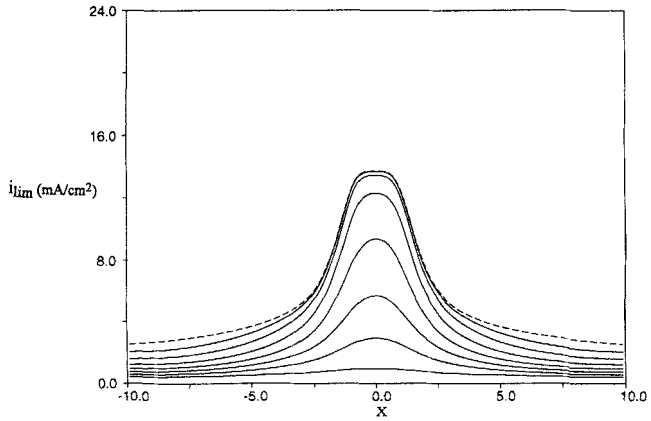

(a)

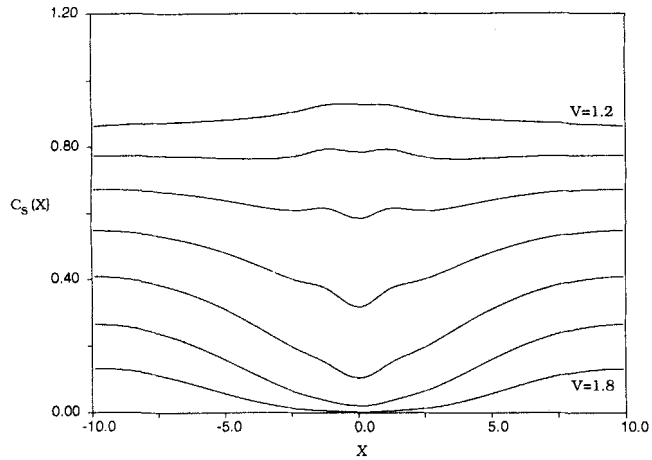

(b)

Figure 6. (a) Current density distribution on the cathode for an unsubmerged normal jet ($H = 1$, Re $= 10^4$); calculated curves are for $V = 1.2$ (0.1) 1.8; and ----- denotes the limiting current. (b) Surface concentration for $V = 1.2$ (0.1) 1.8.

unity, but with increasing V, the concentration of the reacting ion is progressively depleted under the anode. Finally, at $V = 1.8$, the limiting current is almost achieved at $x = 0$. It may be noted that because negative values of c_s are not possible, c_s was arbitrarily set equal to 0.001 whenever a negative value of $c_s(x)$ was produced in the iterative scheme, since it is not feasible to introduce a value of c_s identically zero on the right side of Eq. 48. At higher values of V, the numerical scheme then produces a distribution of $c_s(x)$, which has an increasing region (centered on $x = 0$) of values close to zero.

It is necessary to terminate the calculations at some large finite value of x, denoted here as $x = \pm R$. As shown in Figure 4, the computational boundary C cuts the jet at $x = \pm R$, and on this portion of C, the normal derivative of potential was assumed to vanish as an approximation ($\phi' = \phi_x \approx 0$). In principle, two physical situations may be imagined, one in which the cathode is infinite in extent and one where the cathode has a finite extent of $2R$; for either situation, taking $\phi' = 0$ on the portion of C cutting the jet is an approximation, although this condition is somewhat more realistic in the latter case. Recently Novy et al. (1991) have evaluated various types of outflow conditions and conclude that a Robins-type condition (involving ϕ and ϕ') gives the best results; such a condition was not developed in the present study but might prove useful in future work. For the case of an infinitely long cathode, it is difficult to obtain solutions that are completely independent of R because, although both i and ϕ approach zero for large x, the decay is very slow (cf. Eq. 39). Calculated results for a cathode 100 units long are shown in Figure 7 for the same applied voltages depicted in Figure 6, where the cathode is twenty units long; note that the scale of the two sets of figures is different, but also that the distributions of current density and surface concentration are actually very similar, showing the same type of trends. Because of the strongly global interactive nature of the calculation, some dependence on the position of the outer computational boundaries at $x = \pm R$ must be accepted in the results. It can be noted in Figure 7b that $c_s \to 1$ as $|x| \to \infty$ for large x for all applied voltages, but that $c_s = 1$ is not achieved at $x = \pm R$. Calculations were also carried out for larger val-

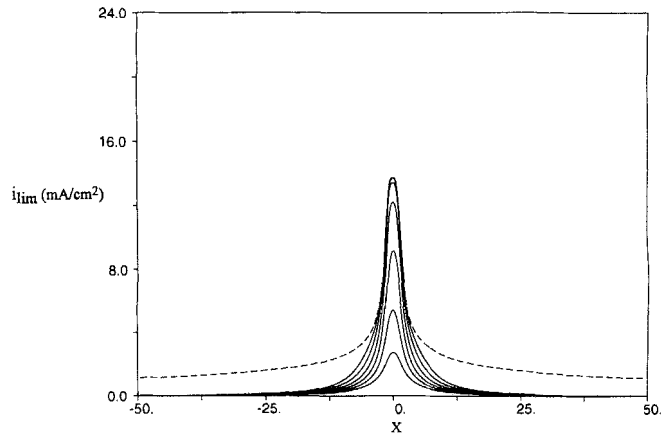

(a)

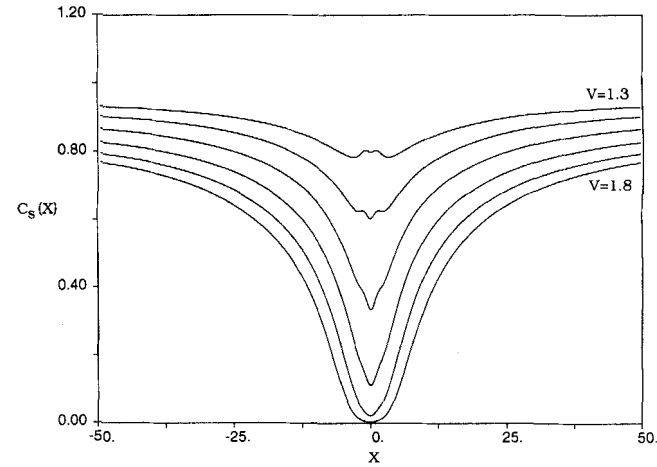

(b)

Figure 7. (a) Current density distribution on the cathode for an unsubmerged normal jet ($H = 1$, Re $= 10^4$); calculated curves are for $V = 1.3$ (0.1) 1.8 for $R = 50$. (b) Concentration distribution for $V = 1.3$ (0.1) 1.8.

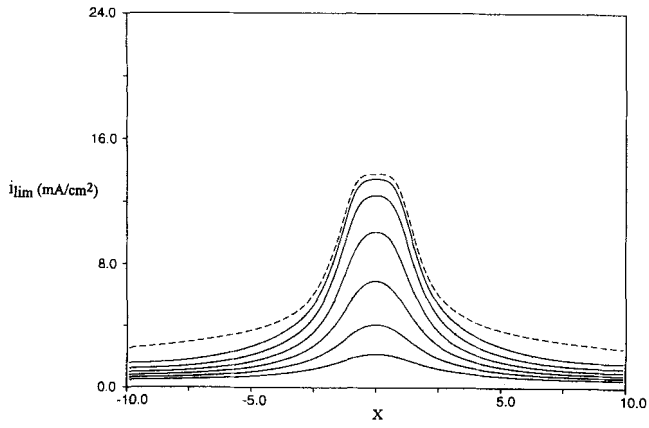

Figure 8. Current density distribution on the cathode for an unsubmerged normal jet ($H = 2$, $Re = 10^4$); calculated curves are for $V = 1.3$ (0.1) 1.8 and ----- denotes the limiting current.

ues of R, and a general trend is that c_s continually increases toward unity at $x = \pm R$. However, the asymptotic approach to 1 is very slow for large x for any given applied voltage. Because it is necessary to invert a full matrix in the boundary element method, as well as maintain a large number of points in the impingement zone (for good accuracy there), it is generally not viable to carry out solutions for extremely large values of R. In a calculation on a modern workstation, about 400 points around the computational boundary is feasible, and generally over half of the points should be devoted to the cathode in a nonuniform mesh with nodes clustered near O.

In Figure 8, the influence of moving the anode further from the wall is depicted. The calculated distributions of current density are quite similar to those shown in Figure 6a. Close comparison of these figures shows that the current density is generally lower for increased H at a given applied voltage. Results for surface concentration are not shown, but are similar to those shown in Figure 6b, except that the limiting current has not quite been achieved for $V = 1.8$.

Calculated results for a submerged normal jet are shown in Figure 9. A comparison with Figure 6 shows that the current density distributions are similar for both the submerged and unsubmerged jets. However, for the unsubmerged jet, the current levels for a given V are higher in the impingement zone near O and lower for larger values of x. Consequently, the unsubmerged jet is somewhat preferable when selectivity is important, since it acts to concentrate the electrodeposition in the impingement zone. Note from Figure 9a and 9b that the limiting current is reached around $V = 1.8$ almost all along the cathode rather than just near $x = 0$ as in Figure 6 for the unsubmerged jet. This general type of behavior was found for all cases of submerged jets considered. Since the results are not dramatically different from those obtained for unsubmerged jets, the submerged case will not be considered further. It is noted in passing that the computational domain for the submerged case is very simple (Figure 4), and thus computations for the submerged jet are much easier to perform.

Now consider the influence of directing the jet at an angle θ to the surface as depicted in Figure 1. Calculated results for angles of 60°, 45°, and 30° are shown in Figures 10 through 12, respectively. It may be seen that as the jet angle θ is decreased, the current density levels near $x = 0$ increase for a given applied voltage, and in addition, the region of high current levels becomes more sharply focused near O. Outboard of the impingement zone, higher levels of current density are also achieved on the surface in front of the jet as opposed to the region behind it, and at $V = 1.8$, the limiting current is almost achieved in front of the jet. This behavior can also be seen in the surface concentration distributions.

Discussion

In the present study, the problem of electrodeposition from an impinging jet has been considered. The present results are broadly consistent with trends observed in various experimental studies of heat transfer (Goldstein and Franchett, 1988), mass transfer (Sparrow and Lovell, 1980), and electrodeposition (Alkire and Chen, 1982; Alkire and Ju, 1987; Chin and Agarwal, 1991) on a surface near an impinging jet. It should be noted that there are differences in the transport processes in the studies just listed, as well as similarities; in addition, the preceding electrodeposition experiments were

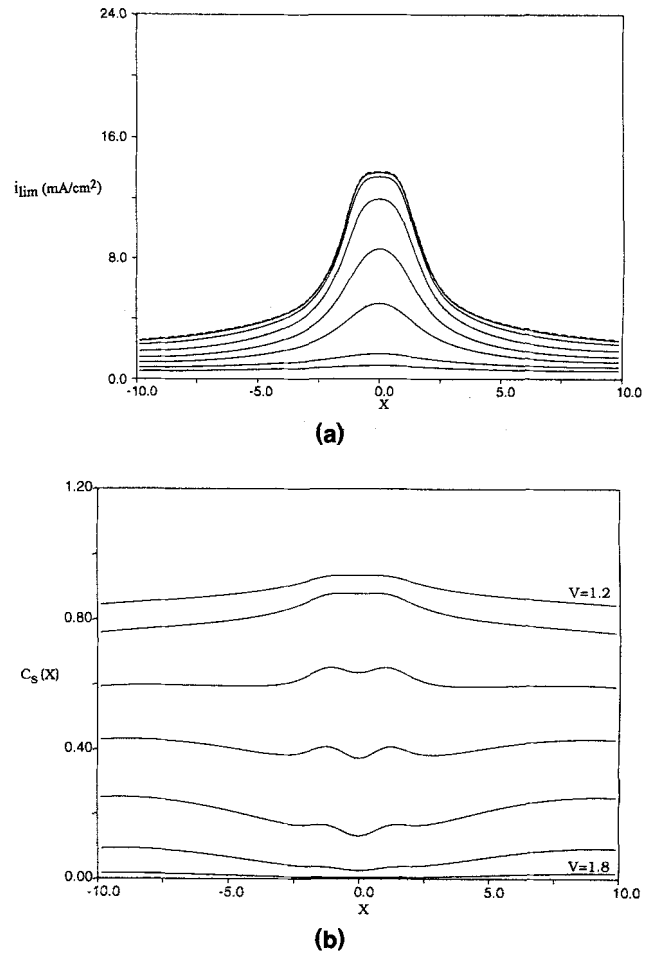

Figure 9. (a) Current density distribution on the cathode for a submerged normal jet ($H = 1$, $Re = 10^4$); calculated curves are for $V = 1.2$ (0.1) 1.8 and ----- denotes the limiting current. (b) Surface concentration for $V = 1.2$ (0.1) 1.8.

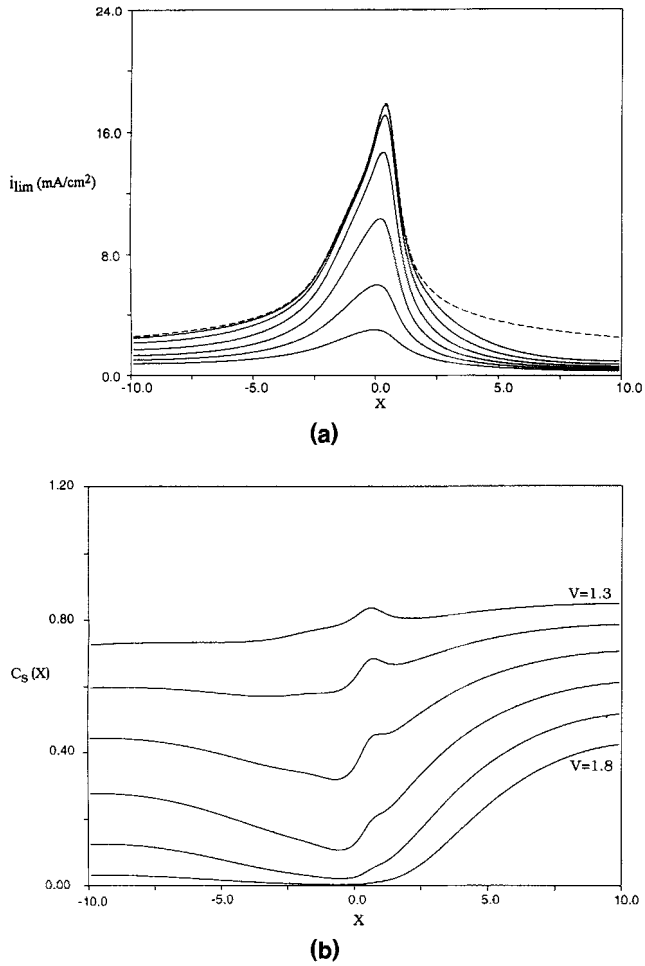

Figure 10. (a) Current density distribution on the cathode for an unsubmerged jet at an angle $\theta = 60°$ ($H = 1$, $Re = 10^4$); calculated curves are for $V = 1.3$ (0.1) 1.8 and ----- denotes the limiting current. (b) Surface concentration for $V = 1.3$ (0.1) 1.8.

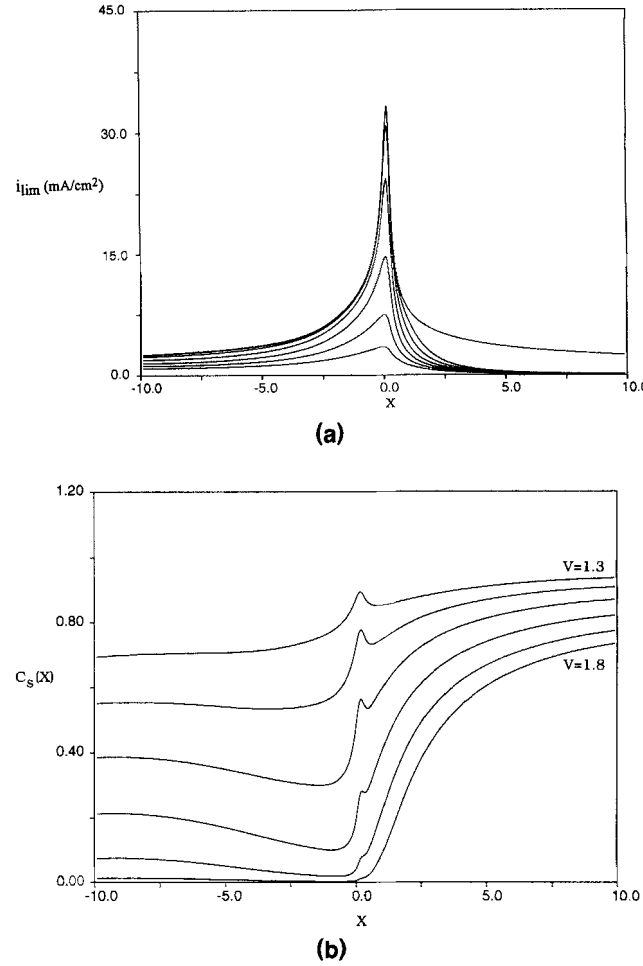

Figure 12. (a) Current density distribution on the cathode for an unsubmerged jet at an angle $\theta = 30°$ ($H = 1$, $Re = 10^4$); calculated curves are for $V = 1.3$ (0.1) 1.8 and ----- denotes the limiting current. (b) Surface concentration for $V = 1.3$ (0.1) 1.8.

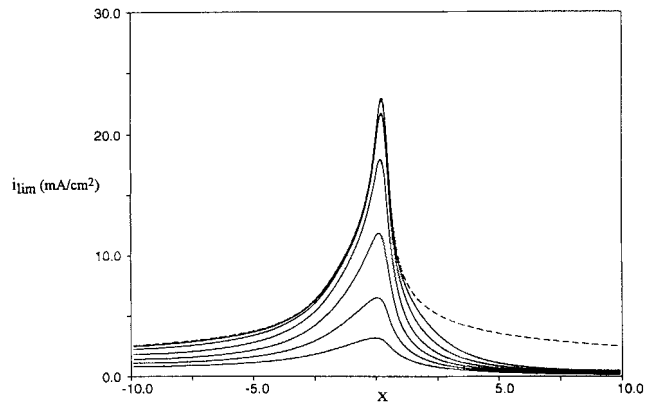

Figure 11. Current density distribution on the cathode for an unsubmerged jet at an angle $\theta = 45°$ ($H = 1$, $Re = 10^4$); calculated curves are for $V = 1.3$ (0.1) 1.8 and ----- denotes the limiting circuit.

generally carried out near the limiting current, while a major focus of the present study is associated with applied voltages that produce current distributions below the limiting current. Nevertheless some general conclusions can be drawn. First, the current density distributions on the cathode are similar for unsubmerged and submerged jets. However, the unsubmerged jet gives somewhat higher current levels near the impingement zone, in agreement with the experiments of Alkire and Ju (1987). At the same time, current levels outside the impingement zone are somewhat lower for an unsubmerged jet and, consequently, this configuration is preferable in situations where selectivity is important. Second, moving the anode closer to the surface results in high current densities in the impingement zone but, as noted by Alkire and Ju (1987), the influence of moving the nozzle further away from the surface is weak. Third, as is evident from Eqs. 36 and 37, an increase in Reynolds number results in an increase in the current at the surface, in agreement with the trends in the experiments of Chin and Agarwal (1991).

Now consider the question of the orientation of the jet relative to the surface. As shown in Figures 6 and 8, the normal jet produces a current density that is almost uniform near the limiting current in a concentrated band near the point of impingement. By orienting the jet at an angle, the most significant current levels are concentrated in a progressively narrower band in the impingement zone. The maximum current level occurs in the lee of the jet; this behavior has clearly been observed in the mass-transfer experiments of Sparrow and Lovell (1980) and Chin and Agarwal (1991), as well as the heat-transfer experiments of Goldstein and Franchett (1988). The streamwise narrowing of the zone of high surface flux with decreasing jet angle is also evident in the experiments of Chin and Agarwal (1991), and especially so in those of Goldstein and Franchett (1988). When the jet is oriented at an angle, the high electrodeposition rates in a relatively narrow region are reflective of the behavior of the viscous shear near the surface. In such situations, the variation in the mainstream velocity outside the boundary layer is very intense near the impingement point as shown in Figure 2; this results in a sharp variation in the shear stress near impingement, especially in the lee of the jet, as shown in Figure 3. Relatively high values of shear stress then give rise to enhanced levels of electrodeposition. As shown in Figure 5 for the limiting current, as well as in Figures 10–12 for the current distributions, the peak values of the current increase with decreasing jet angle θ. This phenomenon can be observed in the experimental results of Goldstein and Franchett (1988) and Chin and Agarwal (1991) as θ decreases from 90° toward 45°. It may be noted that the trend does not seem to continue in the experimental results as θ decreases to still lower values. However, as indicated in Figure 5, the region of high surface flux becomes concentrated in a progressively narrower streamwise band as θ decreases. For this reason the maximum flux may be very difficult to determine accurately in experiments unless measurements are carried out with very high spatial resolution near the impingement zone. Of course, it is not possible to increase the sharpness of the effective plating zone indefinitely by continually decreasing θ. For small θ, the width of the wall jet to the right in Figure 1 eventually approaches zero, and the present theory does not apply. The present calculations indicate that selective plating can be carried out over a relatively narrow band on the cathode when the jet is oriented at moderate angles to the surface.

Finally, it may be noted that in many situations (see, for example, Chin and Agarwal, 1991) the jet and boundary layer downstream of the impingement zone become turbulent; this phenomenon gives rise to sharp local increases in the Sherwood number (Chin and Agarwal, 1991) outboard of the impingement zone. Turbulence is not accounted for in the present formulation, and it is worthwhile to assess the relevance of the present analysis, which is based on laminar flow. Turbulence may occur in either the jet itself or within the boundary layer on the cathode. Unfortunately, established results for the stability and transition in jets oriented in the present configuration are not available. For a thin submerged jet issuing into an otherwise stagnant fluid, Schlichting (1979) indicates that laminar flow persists only up to $Re = 30$. However, the present study mainly concerns thick unsubmerged jets, and in the experiments of Chin and Agarwal (1991), the jet was believed to be laminar at the stagnation point in the Reynolds number range considered of $Re = 1{,}000$–$7{,}000$. In any event, the inviscid solution used in the present study is also believed to be a reasonable model for a thick turbulent jet. The treatment of the boundary layer is of greater concern since Chin and Agarwal (1991) observed transition occurring somewhere from 4 to 8 jet diameters outboard of the stagnation point. In principle, this behavior should be accounted for, thereby necessitating implementation of some type of transition and turbulence models. Due to the global nature of the calculation, boundary-layer transition will have an effect on the final results; however, it is not believed to have a significant influence on predicted electrodeposition rates in the impingement zone, especially for situations near the limiting current. As shown in Figures 6–12, the limiting current is first achieved at the impingement point; with increasing applied voltage the surface concentration is gradually reduced toward small values outboard. Transition in the boundary layer can therefore only result in a limited local increase in current and certainly not to be levels achieved in the impingement zone. At lower applied voltages, turbulence will have a greater impact on the current distribution due to the inherent global interaction that occurs between the electric field and the hydrodynamic, diffusion, and electrochemical layers.

Notation

c_1 = concentration of reacting ion
V_{app} = applied cell potential
$z = x + iy$ = complex variable
ζ = normal coordinate in the diffusion layer (Eq. 29)
ξ = longitudinal coordinate in the diffusion layer

Literature Cited

Acrivos, A., "Solution of the Laminar Boundary Layer Energy Equation at High Prandtl Numbers," *Phys. Fluids*, **3**, 657 (1960).

Albery, W. J., "The Current Distribution on a Wall-Jet Electrode," *J. Electroanal. Chem.*, **191**, 1 (1985).

Alkire, R. C., and T.-J. Chen, "High Speed Selective Electroplating with Single Circular Jets," *J. Electrochem. Soc.*, **129**, 2424 (1982).

Alkire, R. C., and J.-B. Ju., "High Speed Selective Electroplating with Impinging Two-Dimensional Slot Jet Flow," *J. Electrochem. Soc.*, **134**, 294 (1987).

Bindra, P., D. Light, P. Freudenthal, and D. Smith, "The Effect of Base Metal Ions on the Electrochemical and Structural Characteristics of Electrodeposited Gold Films," *J. Electrochem. Soc.*, **136**, 3616 (1989).

Caban, R., and T. W. Chapman, "Rapid Computation of Current Distribution by Orthogonal Collocation," *J. Electrochem. Soc.*, **123**, 1036 (1976).

Cebeci, T., and A. M. O. Smith, *Analysis of Turbulent Boundary Layers*, Academic Press, New York (1974).

Cheh, H. Y., and R. Sard, "Electrochemical and Structural Aspects of Gold Electrodeposition from Dilute Solutions by Direct Current," *J. Electrochem. Sci.*, **118**, 1737 (1971).

Chin, D.-T., and M. Agarwal, "Mass Transfer from an Oblique Impinging Slot Jet," *J. Electrochem. Soc.*, **138**, 2643 (1991).

Glauert, M. B., "The Wall Jet," *J. Fluid Mech.*, **1**, 625 (1956).

Goldstein, R. J., and M. E. Franchett, "Heat Transfer from a Flat Surface to an Oblique Impinging Jet," *J. Heat Transfer, Trans ASME*, **110**, 84 (1988).

Gray, L. J., "A Note on Overhauser Elements," *Boundary Elem. Commun.*, **5**, 62 (1994).

Gray, L. J., and L. L. Manne, "Hypersingular Integrals at a Corner," *Eng. Anal. Boundary Elem.*, **11**, 327 (1993).

Jaswon, M. A., and G. T. Symm, *Integral Equation Methods in Potential Theory and Electrostatics*, Academic Press, New York (1977).
Kim, H.-D., and J. D. A. Walker, "Computer Prediction of Electroplating Rates on Metal Electrodes," Rep. FM-12, Lehigh University, Bethlehem, PA (1988).
Lighthill, M. J., "Contributions to the Theory of Heat Transfer through a Laminar Boundary Layer," *Proc. R. Soc. London A*, **202**, 359 (1950).
Milne-Thomson, L. M., *Theoretical Hydrodynamics*, 4th ed., Macmillan, New York (1962).
Newman, J. S., *Electrochemical Systems*, 2nd ed., Prentice-Hall, Englewood Cliffs, NJ (1991).
Newman, J. S., "The Effect of Migration in Laminar Diffusion Layers," *Int. J. Heat Mass Trans.*, **10**, 983 (1967).
Novy, R. A., H. T. Davis, and L. E. Scriven, "A Comparison of Synthetic Boundary Conditions for Continuous-Flow Systems," *Chem. Eng. Sci.*, **46**, 57 (1991).
Parrish, W. R., and J. S. Newman, "Current Distribution on a Plane Electrode Below the Limiting Current," *J. Electrochem. Soc.*, **116**, 169 (1969).
Pickett, D. J., *Electrochemical Reactor Design*, 2nd ed., Elsevier, New York (1979).
Schlichting, H., *Boundary Layer Theory*, McGraw-Hill, New York (1979).
Smith, G. D., *Numerical Solution of Particle Differential Equations: Finite Difference Methods*, 3rd ed., Oxford Univ. Press, Oxford (1985).
Sparrow, E. M., and B. J. Lovell, "Heat Transfer Characteristics of an Obliquely Impinging Circular Jet," *J. Heat Transfer, Trans ASME*, **102**, 202 (1980).
Vetter, K. J., *Electrochemical Kinetics, Theoretical Aspects*, Academic Press, New York (1967).
Walker, J. D. A., and G. G. Weigand, "An Accurate Method for Two-Point Boundary Problems," *Int. J. Num. Meth. Engr.*, **14**, 1335 (1979).
Werle, M. J., and R. T. Davis, "Incompressible Boundary Layers on a Parabola at Angle of Attack: a Study of the Separation Point," *Trans. ASME Ser. E., J. Appl. Mech.*, **39**, 7 (1972).
White, F. M., *Viscous Fluid Flow*, 2nd ed., McGraw-Hill, New York (1992).
Yamada, J., and H. Matsuda, "Limiting Diffusion Currents in Hydrodynamic Voltamometry. III. Wall Jet Electrodes," *J. Electroanal. Chem.*, **44**, 189 (1973).

Manuscript received Apr. 28, 1994, and revision received Apr. 6, 1995.